Mon. Not. R. Astron. Soc. **000**, 1–14 (2005) Printed 20 December 2007 (MN LaTeX style file v2.2)

2-D Monte Carlo simulations of H I line formation in massive YSO disk winds

S. A. Sim⋆[1], J. E. Drew[1], K. S. Long[2]
[1]*Astrophysics Group, Imperial College London, Blackett Laboratory, Prince Consort Road, London, SW7 2AZ, UK*
[2]*Space Telescope Science Institute, 3700 San Martin Drive, Baltimore, MD 21218, USA*

3 August 2005

ABSTRACT
Massive young stellar objects (YSOs) are powerful infrared H I line emitters. It has been suggested that these lines form in a outflow from a disk surrounding the YSO. Here, new two-dimensional Monte Carlo radiative transfer calculations are described which test this hypothesis. Infrared spectra are synthesised for a YSO disk wind model based on earlier hydrodynamical calculations. The model spectra are in qualitative agreement with the observed spectra from massive YSOs, and therefore provide support for a disk wind explanation for the H I lines. However, there are some significant differences: the models tend to overpredict the Brα/Brγ ratio of equivalent-widths and produce line profiles which are slightly too broad and, in contrast to typical observations, are double-peaked. The interpretation of these differences within the context of the disk wind picture and suggestions for their resolution via modifications to the assumed disk and outflow structure are discussed.

Key words: radiative transfer – methods: numerical – stars: early-type – stars: winds, outflows

1 INTRODUCTION

Understanding the formation and pre-main-sequence evolution of massive stars ($M \gtrsim 10$ M$_\odot$) is an important goal in modern astrophysics. Currently, the formation of low-mass stars via gravitational collapse of a molecular cloud and subsequent disk accretion is, at least conceptually, well understood but it is not clear whether massive stars form through a scaled-up version of the same process or whether more complex, environmental effects are important (see e.g. Bonnell, Vine & Bate 2004 for a recent discussion).

Since massive stars form inside dense molecular clouds, they are observed primarily at infrared (IR) and longer wavelengths. Embedded massive YSOs are powerful sources of IR H I line emission (Simon et al. 1981, 1983; Drew, Bunn & Hoare 1993; Bunn, Hoare & Drew 1995; Blum et al. 2004) with equivalent widths (EWs) in Brα of $\sim$ 5 – 90 Å (Bunn et al. 1995). The lines profiles are complex, displaying both fairly narrow (full-width-at-half-maximum [FWHM] $\sim$ 50 – 100 km s^{-1}) line cores and broad wings extending out to $\sim$ 400 km s^{-1} in extreme cases. In the sample of objects observed by Bunn et al. (1995), the profiles were always single-peaked but recent observations reported by Blum et al. (2004) include at least one object (NGC 3576) which shows clear evidence of double-peaked profiles. By examining flux ratios across the profiles of lines with differing opacities, Bunn et al. (1995) found evidence that, at least in some sources, the lines form in an accelerating outflow.

Normal, main-sequence OB stars also show H I emission lines. These are produced in the star's fast ($\sim$ 1000 km s^{-1}) spherical wind, but the strength of emission in YSO spectra is much greater than in O-stars. If the features in YSOs were due to reprocessing of radiation in a spherically symmetric wind, the implied mass-loss rates would be up to 10^{-6} M$_\odot$ yr^{-1} (Simon et al. 1983), substantially exceeding those of field stars of comparable spectral type. Therefore, to interpret the H I observations it is worthwhile to consider alternatives to formation in a spherically symmetric structure.

Important observational constraints on the geometry of emitting material in YSOs are provided by the first overtone bands of CO at 2.3μm (e.g. Carr 1989; Carr et al. 1993; Chandler et al. 1993; Chandler, Carlstrom & Scoville 1995). In particular, both Carr et al. (1993) and Chandler et al. (1995) conclude that models based on an accretion disk surrounding the central object reproduce the CO observations of YSOs. Furthermore, although there are some cases in which CO data can be modelled in terms of a stellar wind, in general the disk model encounters fewer difficulties (see Chandler et al. 1995). The observations strongly suggest that the CO emission originates close to the central star: Bik & Thi (2004) and Blum et al. (2004) have recently studied CO emission from a range of massive YSOs and derived disk radii in the range 0.1 – 5 AU. Thus it seems probable that YSOs harbour accretion disks containing significant amounts of hot gas fairly close to the central object and it is natural to consider whether the H I emission is associated with such a disk or its environment.

Hamann & Simon (1986) suggested that powerful recombination line emission of the sort discussed above originates in an

⋆ s.sim@imperial.ac.uk

outflow associated not with a stellar wind but with mass-loss from a disk. Their work focused on MWC 349, an object whose evolutionary status is unclear but which possesses spectroscopic signatures (including H I and CO emission features) broadly similar to the embedded massive YSOs (see Hamann & Simon 1986; Kraus et al. 2000). Hollenbach et al. (1994) developed a model for outflow from young massive stars by photoevaporation of the outer regions of their disks. They were motivated by the need to explain the high frequency of occurrence of ultracompact H II regions – photoevaporation can provide a source of mass input for H II regions to balance the loss by pressure-driven expansion. Although the rate of mass-loss in photoevaporation models is large, it occurs at large radii (typically > 100 AU) and the characteristic flow velocities are low (comparable to the typical sound speed of 10 – 50 km s^{-1}, Hollenbach et al. 1994). Thus, such a flow does not provide a promising origin for relatively high velocity features, such as the IR H I broad line wings (Bunn et al. 1995).

Recently, Drew, Proga & Stone (1998) proposed that the intense radiation field produced by a massive YSO may drive mass-loss from the surface of the inner parts of its disk. They performed a hydrodynamical simulation which showed that, in addition to driving a normal hot star wind component, radiation pressure from a massive YSO could propel a dense equatorial flow from a surrounding disk with terminal velocity in the same regime as the observed H I linewidths. These results led them to speculate that such a model accounts for the IR H I lines. However, they did not perform the radiative transfer calculations required to confirm this conjecture.

To investigate the possibility that massive YSOs harbour disk winds which give rise to the observed IR H I line emission, this paper presents the results of new two-dimensional radiative transfer calculations which account for both the complex geometry of a YSO disk wind (starting from, but not limited to, the Drew et al. 1998 model) and the detailed atomic physics of H I line formation.

In Section 2, the YSO model adopted in this investigation and its parameters are discussed. The radiative transfer calculations have been performed using the Monte Carlo (MC) code described by Long & Knigge (2002) after incorporating a sophisticated treatment of H I line formation using the approach described by Lucy (2002,2003); the method of calculation and code used are discussed in Section 3. Results are presented in Section 4 and our conclusions discussed in Section 5.

2 MODEL

For the radiative transfer calculations (Section 4) a simply parameterised model for the YSO and its disk is adopted. In choosing the parameters for this model, our starting point has been to construct a reasonable representation of the disk wind obtained in the hydrodynamical simulations presented by Drew et al. (1998). Therefore, before discussing our model in detail, a brief description of this hydrodynamical model is given.

2.1 Summary of the hydrodynamical disk wind model

Following the methods of Proga et al. (1998), Drew et al. (1998) performed a hydrodynamical simulation of a radiatively driven wind from a disk around a massive YSO. They considered an early-B type star (mass $M_* = 10$ M$_\odot$, luminosity $L_* = 8500$ L$_\odot$, radius $r_* = 5.5$ R$_\odot$) surrounded by an accretion disk extending from the stellar surface to an outer radius $r_{\rm disk} = 10\ r_*$, the outer boundary of their computational domain. Noting that, for reasonable accretion rates ($\sim 10^{-6}$ M$_\odot$ yr^{-1}), the luminosity of the central star far exceeds the accretion luminosity of the disk, they accounted for reprocessing of stellar light by the disk and then computed the radiation force using the Castor, Abbott & Klein (1975) parameterisation of the force due to spectral lines.

Their simulation exhibited a steady state solution with two fairly distinct outflow components: a fast (~ 2000 km s^{-1}) polar wind from the central star, rather similar to a normal hot star wind; and a slower (< 400 km s^{-1}), denser equatorial outflow from the disk at colatitude $\theta \sim 60°$ with mass-loss rate $\sim 3\times10^{-8}$ M$_\odot$ yr^{-1}. Between these two outflow components they found a complex transitional zone in which the stellar wind streamlines were compressed due to non-radial radiation force components and the presence of the disk wind.

Drew et al. (1998) suggested that the high density and moderate velocity of the equatorial disk-wind component make it a promising site for the formation of the H I lines observed in massive YSO spectra – our goal is to present radiative transfer calculations to examine this hypothesis.

2.2 Geometry

Figure 1 illustrates the geometrical construction used to describe the wind, parameters for which are discussed in the next subsection. In order to capture the essence of the Drew et al. (1998) hydrodynamical disk wind model (described above), the structure consists of the following four basic elements:

(i) A central star. The star is assumed to be spherical with radius r_*.

(ii) An accretion disk. The disk lies in the xy-plane of the adopted coordinate system and is assumed to extend from the surface of the star to an outer radius $r_{\rm disk}$. For simplicity, it is assumed to be geometrically thin and flat.

(iii) A disk wind. The wind, which is launched from the disk, is described following Long & Knigge (2003) and Knigge, Woods & Drew (1995): namely the streamlines of the disk wind are assumed to converge at a point which lies on the z-axis a distance d below the coordinate-origin. Thus the angular boundaries of the disk wind are determined by the choice of the inner and outer disk radii and the distance d; namely $\theta_{\rm min} = \tan^{-1}(r_*/d)$ and $\theta_{\rm max} = \tan^{-1}(r_{\rm disk}/d)$(see Figure 1). Motivated by the Drew et al. (1998) simulation, the flow is assumed to be stationary and smooth.

(iv) A spherical stellar wind component. This is assumed to occupy the entire polar region above the disk wind and to have radial streamlines. The boundary between the stellar wind and disk wind is not treated in detail; it is assumed to be perfectly sharp – thus the transition zone between the disk and stellar winds which exists in the Drew et al. (1998) simulation is neglected here.

2.3 Model parameters

Table 1 gives a list of the wind parameters adopted for the reference model (hereafter, Model A) which are discussed individually below. Of our models, Model A and the closely related Model B (see Section 4.3) are those most closely matching the Drew et al. (1998) simulation.

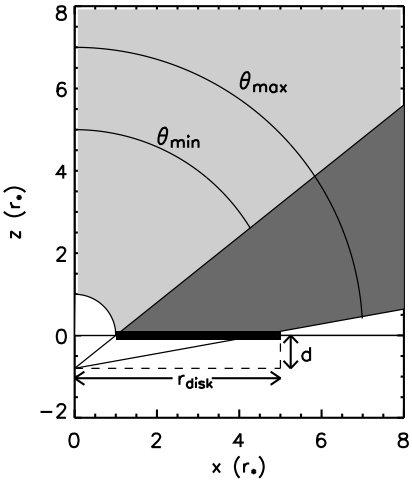

Figure 1. The elements of the geometrical construction used to define the wind (only the positive xz-plane is shown – the wind is symmetric about both the xy-plane and the z-axis). The quarter-circle line around the origin represents the stellar surface; the stellar wind is shaded light grey, the disk wind dark grey and the disk black. The equatorial region beyond the disk (white) is assumed to be empty. The figure is *not to scale* for the parameters given in Table 1.

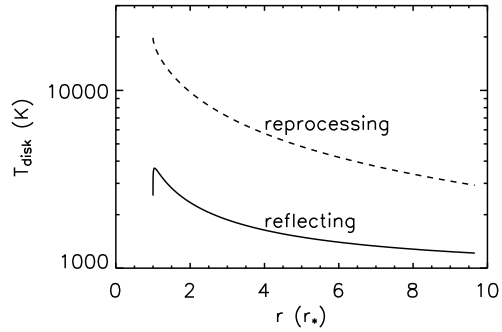

Figure 2. The disk temperature ($T_{\rm disk}$) as a function of radius (r) for a reflecting disk (solid line) and a reprocessing disk (dashed line). The reflecting disk temperatures are always lower since they only describe the accretion luminosity while the reprocessing disk also accounts for re-radiation of energy absorbed from the star.

2.3.1 Central star

The parameters of the central star are those of a B1-B2 main sequence star. The effective temperature was computed from the luminosity using the Stefan-Boltzmann equation. The star is assumed to emit radiation as a black body.

2.3.2 Accretion disk

In our reference model, $r_{\rm disk} = 10\ r_*$ is adopted – the same computational domain considered by Drew et al. (1998). Realistically, the disks around massive YSOs are likely to extend to significantly larger radii. Therefore, we will also consider disks extending to $r_{\rm disk} = 100\ r_*$ in Section 4. To consider even larger radii becomes impractical since increasing the physical size of the calculation limits the spatial resolution available in the inner regions – computing feasibility prevents us from having arbitrarily many grid cells. It is noted that, at least for the treatment of disk radiation adopted in our reference model, considering an even larger outer radius will have negligible effect – the disk temperature at such large radii will be too low for its thermal radiation to contribute significantly to the IR spectral range under consideration.

Given that it lies considerably beyond the scope of this investigation to study radiative transfer within the accretion disk in detail, approximations must be made regarding the treatment of the disk and its emission. In the calculations presented in Section 4, results using two different approaches are considered. It is known from observations (Henning, Pfau & Altenhoff 1990) that there are significant differences in the IR SEDs of massive YSOs – some have large near-IR excesses while other have little or no excess. Therefore, we have chosen our two models for disk emission to approximately bracket the range of plausible IR SEDs for massive YSOs.

In some cases, referred to as a "reflecting" disk, it is assumed that the disk effective temperature is determined as a function of radius by the accretion rate (exactly as discussed by Long & Knigge 2002) and that annuli of the disk emit as black bodies at the local temperature. During the MC simulations, it is assumed that any radiation which strikes the disk from above is reflected by a hot disk atmosphere rather than absorbed and reprocessed. Since the computational domain is symmetric about the disk plane, this is closely equivalent to the assumption that the disk is completely optically thin (transparent). In Model A, the disk is assumed to be "reflecting".

Alternatively, as a simple "reprocessing" disk model, it is assumed that stellar radiation falling on the disk is absorbed and the energy re-radiated. In this case, the disk is divided into concentric annuli and the energy falling on each annulus from the star computed following the discussion of Proga et al. (1999). By assuming that all this energy is re-radiated locally, and that the annuli radiate as black bodies, the disk temperatures are then obtained. The accretion luminosity is still included in this model but is small relative to the reprocessed luminosity. At the start of the MC simulation, the disk annuli emit black-body radiation according to their effective temperatures – thereby accounting for the luminosity due to reprocessing of stellar light – and during the subsequent propagation of MC quanta, any radiation which strikes the disk is simply absorbed.

Computed disk temperature for both reflecting and reprocessing disks are shown, as a function of radius, in Figure 2. Spectral energy distributions (SED) for radiant energy emitted from models with both reflecting and reprocessing disks are shown in Figure 3. Comparing the SEDs for reflecting and reprocessing disks with $r_{\rm disk} = 10\ r_*$ (left-hand panels in Figure 3) shows that the treatment of the disk makes a significant difference to the continuum brightness in the IR region of interest. If the disk only reflects (or transmits) light which strikes it, the ~ 2 – $4\ \mu$m continuum is a combination of stellar radiation and accretion luminosity released in the disk. (Figure 3, upper-left panel). However, if the disk thermally reprocesses all the stellar light which strikes it, the reprocessed light is dominant (lower-left panel). Increasing the outer radius of the disk to 100 r_* increases its brightness. With a reflecting disk, this effect is fairly small below about 4 μm (upper-right panel) because the temperatures of the outer parts of the disk are very low. However, since the reprocessing disk has higher temperatures (Figure 2), changing its outer radius has a greater effect in the waveband of interest (Figure 3, lower-right panel).

We note that since the treatment of the radiation force is grey

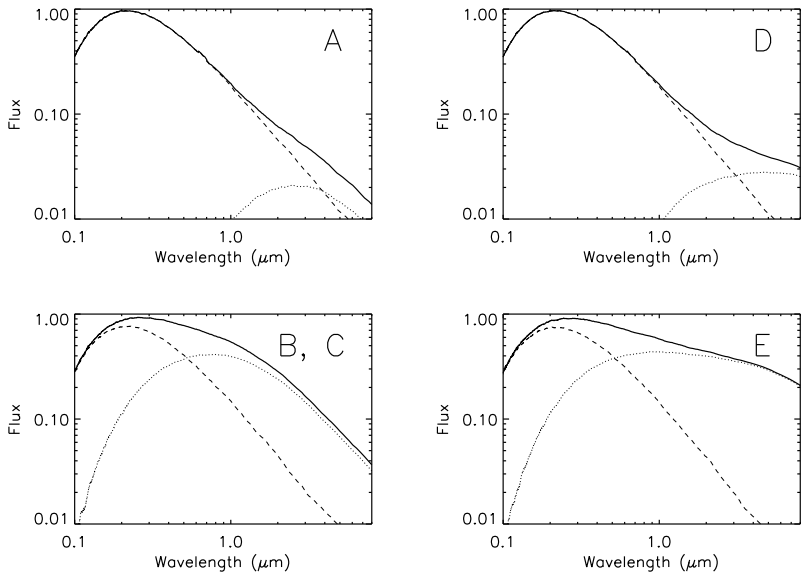

Figure 3. Spectral energy distributions (SED) for models with star and reflecting disk (upper panels) and star and reprocessing disk (lower panels). The left panels are for disks extending to outer radius $r_{\rm disk} = 10\ r_*$ while the right panels are appropriate for $r_{\rm disk} = 100\ r_*$. In each panel, the heavy line shows the complete SED while the dashed and dotted lines show, respectively, the contributions due to the star and disk. The same relative flux scale is used in each plot. The letters given in the upper right corners of the panels indicate in which of the models discussed in Section 4 the SED is adopted.

in the Drew et al. (1998) simulation and that in both our approaches to the disk SED all the radiative flux which falls on the disk is re-emitted locally, both our disk SED models are equally valid in the context of the hydrodynamical calculations.

2.3.3 Disk wind

The geometry of the disk wind is specified by the distance between the origin and the focus point, d (see Figure 1). Here, $d = 0.14\ r_*$ is adopted leading to $\theta_{\rm min} = 82°$ and $\theta_{\rm max} = 89°$ (see above). The dense disk wind component present in the hydrodynamic model of Drew et al. (1998) occupied a rather wider angular range ($\sim 25°$). However, Proga et al. (1999) showed that improved treatment of the radiative line force leads to significantly more swept back equatorial disk winds. In particular, for a model in which the luminosity of the central object substantially exceeds that of the disk (their model E) they found a disk wind with opening angle 8°. Thus the d-value adopted here is chosen to reflect the narrow disk winds obtained by Proga et al. (1999).

The density and velocity structure of the disk wind closely follows that adopted by Long & Knigge (2002). Following equation (7) of Long & Knigge (2002), it is assumed that the mass loss rate per unit area from the disk can be described by

$$\frac{\delta \dot{M}}{\delta A} \propto T_{\rm disk}(r)^{4\alpha} \qquad (1)$$

On the assumption that the mass-loading is proportional to the local luminous flux, $\alpha = 1$ is adopted here. The total mass-loss rate in the disk wind is fixed at the mass-loss rate obtained by Drew et al. (1998): $\dot{M} = 3\times10^{-8}$ M$_\odot$ yr^{-1}. Note that the improved treatment of the line force (i.e. Proga et al. 1999) did not significantly change the total mass-loss rates from those of the earlier treatment. The

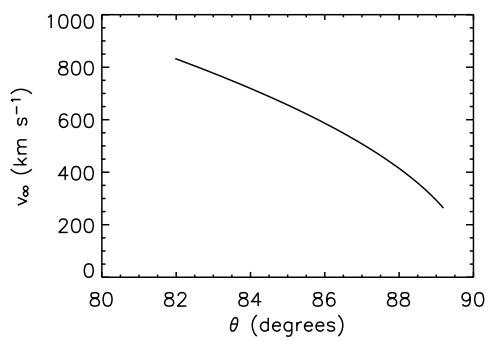

Figure 4. The disk wind terminal velocity (v_∞) versus $\theta = \tan^{-1}(r/d)$ where r is the disk radius at the base of the streamline.

poloidal velocity on a streamline in the disk wind is described using equation (8) of Long & Knigge (2002), namely

$$v(l) = c_s + (v_\infty - c_s)\left(1 - \frac{R_d}{l + R_d}\right)^{\beta_d} \qquad (2)$$

where c_s is the sound speed on the disk surface at the base of the streamline, v_∞ is the terminal velocity of the streamline, l is the poloidal distance, R_d is a velocity-law scale length for the disk wind and β_d is an exponent which determines the acceleration of the wind. For simplicity, $v_\infty = v_{\rm esc}$ is adopted where $v_{\rm esc}$ is the escape velocity on the disk surface at the base of the streamline. Figure 4 shows v_∞ as a function of θ – these values compare favourably with the terminal velocities found by Drew et al. (1998, their figure 3). To describe the acceleration of the wind, a velocity scale length for the disk-wind, $R_d = r_*$ and exponent $\beta_d = 1.5$ are used.

Table 1. Parameters for the reference model (Model A). Parameters for which departures from the reference values will be discussed are indicated with a tick (✓) in the third column.

Parameter	Value	Varied
Central star		
mass, M_*	10 $M_\odot$	
radius, r_*	5.5 $R_\odot$	
luminosity, L_*	8500 $L_\odot$	
temperature, $T_{\rm eff}$	2.37×10^4 K	
Accretion disk		
inner radius, $r_{\rm in}$	r_*	✓
outer radius, $r_{\rm disk}$	10 r_*	✓
accretion rate, $\dot{M}_{\rm acc}$	10^{-6} $M_\odot$ yr^{-1}	
Disk wind		
focus point, d	0.14 r_*	✓
mass-loss rate, $\dot{M}$	3×10^{-8} $M_\odot$ yr^{-1}	✓
mass-loading exponent, α	1	
terminal velocity, v_∞	$v_{\rm esc}$	
acceleration length, R_d	r_*	
acceleration exponent, β_d	1.5	
Stellar wind		
mass-loss rate, $\dot{M}_s$	10^{-8} $M_\odot$ yr^{-1}	
terminal velocity, v_∞	2000 km s^{-1}	
launch velocity, v_c	$10^{-2} v_\infty$	
acceleration exponent, β_s	1	

2.3.4 *Stellar wind*

The density of the stellar wind component is chosen such that it would have mass-loss rate $\dot{M}_s = 10^{-8}$ $M_\odot$ yr^{-1} if it were spherically symmetric. Following e.g. Lucy & Abbott (1993), the velocity in this component is assumed to be radial and given by

$$v = v_c + (v_\infty - v_c)(1 - (r_*/r))^{\beta_s} \quad (3)$$

Based on the Drew et al. (1998) simulations, $v_\infty = 2000$ km s^{-1} is adopted. In addition, $v_c = 10^{-2} v_\infty$ is assumed and $\beta_s = 1$ – a standard value in modelling hot star winds – is chosen.

2.3.5 *Departures from the reference model parameters*

In Section 4, the dependence of the results on several of the important model parameters listed in Table 1 will be investigated. The calculation is, of course, particularly sensitive to the choice of density in the wind. The density in turn is sensitive to many of the model parameters – most fundamentally, the mass-loss rates which determine the mass-loading of the stellar and disk winds. However, the velocity-law parameters (e.g. v_∞, R_d and β_d) also play a significant role, as does the geometry of the disk wind (determined by d). In Section 4, models with density higher than that in Model A will be considered: these are created by increasing the mass-loss rate only – physically this is the parameter which leads to a simple increase in density everywhere in the wind – but it should be noted that there is a degree of degeneracy between this and the other parameters mentioned above.

The second departure from the reference model (Model A) that will be discussed in Section 4 is an increase in the outer disk radius, $r_{\rm disk}$. The relevance of this parameter to the determination of the disk SED has already been discussed (see Section 2.3.2 and Figure 3).

Finally, a model in which an inner hole is introduced to the accretion disk will be considered. In addition to increasing $r_{\rm in}$ for this model, the d-value is changed in order to preserve the same opening angles ($\theta_{\rm min}$ and $\theta_{\rm max}$) for the disk wind.

Departures of the other parameters from their reference values will not be considered here. For this investigation we wish to restrict ourselves to central objects with parameters suitable for early-type near-main-sequence stars – thus we do not consider models with large values of r_*. An increase in the stellar radius, r_* would mimic many of the effects associated with the introduction of an inner hole to the disk since both push the wind out to regions where the rotational velocity is lower. Thus, our model with an inner hole can be regarded as a proxy for some of the most important consequences of an enlarged central star.

An increase in the stellar luminosity would clearly affect the SED, but could also change the mass-loss rate and possibly the wind geometry – further hydrodynamical calculations would be required to fully investigate results for a range of luminosities. The mass-accretion rate ($\dot{M}_{\rm acc}$) is relevant only to calculations with reflecting disks – in such cases, $\dot{M}_{\rm acc}$ plays an important role in determining the disk temperature and IR SED. For reprocessing disks, these are controlled by the stellar radiation field and $\dot{M}_{\rm acc}$ plays only a minor role. It is very difficult to reliably obtain $\dot{M}_{\rm acc}$ by observation or theory and so we restrict ourselves to considering only one value, that used by Drew et al. (1998).

2.4 Atomic data

For simplicity, it is assumed that both the disk wind and stellar wind consist entirely of hydrogen. An atomic model with energy levels for principle quantum number $n = 1$ to 20 and the continuum state is used in the calculations. Bound-bound oscillator strengths are taken from Menzel & Pekeris (1935). Bound-bound collision rates are derived from the oscillator strengths using the van Regemorter (1962) formula. Photoionization rates are taken from TOPBASE (Cunto et al. 1993) and collisional ionization rates are computed using equation 5-79 from Mihalas (1978). In addition to these processes associated with atomic hydrogen, free-free absorption and emission by H II ions and Thompson scattering by free-electrons are included in the calculations. All other processes are neglected.

3 METHOD OF CALCULATION

In the disk wind model, the IR H I line formation is expected to be driven by recombination of ionised hydrogen gas fairly close to the central star. The observed line ratios (e.g. Bunn el al. 1995) indicate, however, that the line emission is not optically thin making it necessary to perform detailed non-LTE radiative transfer calculations to reliably model the line formation process.

The radiative transfer calculations discussed in the next section were performed using a modified version of the MC code written by Long & Knigge (2002). Since the code has been described in detail elsewhere, only a brief overview and discussion of the important modifications made for this investigation are presented here (see Long & Knigge 2002 for further details of the code).

To synthesise spectra, the code performs a sequence of MC radiative transfer calculations. The code uses indivisible energy packets as the elementary MC quanta, assumes radiative, statistical and

thermal equilibrium in the wind, and utilises a Sobolev treatment of bound-bound transitions.

The code presented by Long & Knigge (2002) adopted a two-level approximation in the treatment of line scattering and used approximate excitation and ionization formulae for the computation of level emissivities. These approximations made the code efficient and thus able to handle a large set of atomic data for many chemical elements. However, the two-level approximation also meant that it was not suitable for modelling lines formed by non-resonance scattering or recombination.

Since the IR H I lines form primarily by recombination, the code has been substantially modified to incorporate recently developed MC radiative transfer techniques which allow the formation of such lines to be modelled. In particular, *Macro Atoms*, as devised and tested by Lucy (2002,2003), are used. This approach allows the radiative equilibrium constraint to be rigorously enforced at all times without approximation in the treatment of interactions between radiation and matter.

Initially, several MC simulations are performed to compute the temperature and degrees of excitation and ionization throughout the wind. For these "ionization cycles" the MC quanta are launched with frequencies spanning a wide enough range to simulate all the important radiative energy inputs to the system. During each of these MC simulations, estimators for the radiative heating rate (e.g. due to photoionization) are recorded in each grid cell. At the end of the simulation, these rates are balanced against cooling rates to determine the local electron temperature which is then adopted in the next simulation. This process is repeated until essentially all grid cells pass a chosen convergence threshold in electron temperature.

For this work, the code has been modified to also record high precision MC estimators for the individual radiative rates (photoionization and bound-bound excitation) following Lucy (2003). At the end of each ionization cycle, these are used, together with the various collision rates and radiative decay rates, to compute level populations and the ionization fraction in each grid cell. These populations are used in the next iteration, alleviating the need to use the approximate analytic formulae for ionization and excitation employed by Long & Knigge (2002). No convergence criterion is enforced for the level populations at present. Lucy (2002) has shown that, provided the populations of the lowest levels are estimated sensibly, the indivisible-energy-packet MC method produces highly accurate emissivities even if the populations for the emitting upper levels are relatively poorly known. This insensitivity motivates our use of the MC method since it substantially reduces our reliance on detailed calculation of excited level populations for an adequate non-LTE investigation of recombination line formation. We note that our convergence criterion on the electron temperature implies a corresponding convergence in the energy flow between the radiation field and the thermal energy pool. Since this energy flow is a summation of all the radiative heating processes in the hydrogen model, its behaviour implies good convergence amongst all the processes which are energetically important.

After the "ionization cycles", a set of additional MC simulations are performed to compute the spectrum (the "spectral cycles"). During these cycles the MC quanta are created in only a fixed frequency interval while the thermal, ionization and excitation states of each grid cell are fixed to the values previously determined as described above. By tracking the quanta, we compute the spectrum as seen by observers at different inclination angles in the frequency range of interest.

In all the calculations described below, the model structure and radiation field properties are discretized onto a two-dimension (r-z) grid consisting of 3000 cells. During each MC calculation, the input radiative energy (which arises from the star and accretion disk) is divided into 3×10^6 indivisible quanta.

We have explicitly verified that our approach is adequate for the calculation of the spectrum by comparing results for models with identical input parameters using smaller and larger numbers of grid cells. These calculations differed by at most a few per cent in the computed H I line strengths from the standard (3000 cell) case. This implies that the number of packets, number of grid cells and the quality of the MC estimators are all sufficient for calculations to this degree of accuracy.

Table 2. The observed range of properties of massive YSO H I IR lines in the sample discussed by Bunn et al. (1995). Note that in several of the objects, Brγ and/or Pfγ are not observed and so the range of EW for these lines is biased towards the brighter sources compared with Brα.

Line	$-$EW (Å)	FWHM km s^{-1}	HWZI km s^{-1}
Brα	4.8 – 87	55 – 155	50 – 415
Brγ	2.4 – 23	70 – 150	70 – 270
Pfγ	2.3 – 12	110 – 150	40 – 260
	EWR		EWR
Brα/Brγ	1.1 – 4.4	Brα/Pfγ	3.0 – 7.2

4 RESULTS

4.1 Observational constraints

Early observations of IR H I emission lines in massive YSOs (e.g. Simon et al. 1981) had insufficient signal-to-noise ratio to provide detailed information on the line shapes, thus subsequent theoretical work (e.g. Höflich & Wehrse 1987) was concerned primarily with modelling the observed line fluxes and flux ratios.

More recently, higher quality data (e.g. Drew et al. 1993, Bunn et al. 1995) has allowed the line shapes to be studied in greater detail in several massive YSOs. In common with earlier work (e.g. Simon et al. 1981,1983; Drew et al. 1993), Bunn et al. (1995) observed a moderately strong, pure-emission line of Brα in all of their targets. In most cases, they also reported weaker emission in Brγ and Pfγ. Their observed line profiles are single peaked and not shifted from the expected local rest velocity by more than a few km s^{-1}. Many of the profiles show line wings which extend to several hundred km s^{-1} from line centre and in some cases these wings are clearly asymmetric. By considering wavelength-dependent line ratios (following Drew et al. 1993), Bunn et al. (1995) found evidence, in at least some cases, of hybrid profiles consisting of a narrow line core (which may have a nebular origin) and broad wings in which the line ratio is consistent with formation in an accelerating outflow.

High resolution observations of several massive YSOs have very recently been presented by Blum et al. (2004). Interestingly, in their sample, at least one object (NGC 3576) has double-peaked, narrow line profiles. However, it is difficult to study the broad line wings in the Blum et al. (2004) data since the spectral coverage is too narrow to establish the underlying continuum with certainty.

In the following sub-sections, results of our models will be compared primarily with the observations presented by Bunn et al. (1995) since their spectra provide good constraints on both line strengths and shapes for a significant sample of objects. Unfortu-

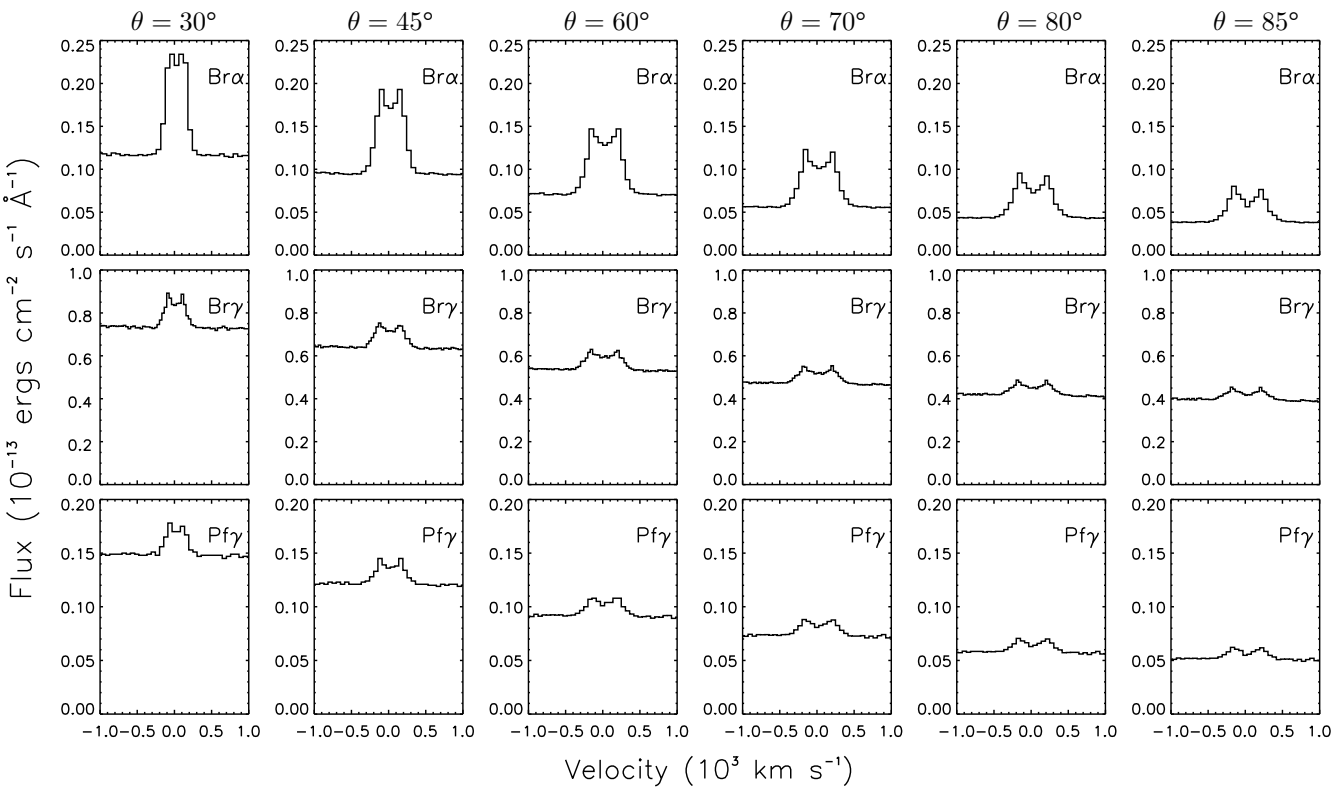

Figure 5. Model A (reference model with reflecting disk): computed Brα (upper), Brγ (centre) and Pfγ (lower) line profiles for viewing angles to the polar axis (from left to right) of 30°, 45°, 60°, 70°, 80° and 85°. The flux is given for an unreddened source at a distance of 1 kpc and the velocity is measured relative to line centre.

nately, owing to the great difficulty in establishing the extinction along the line of sight to massive YSOs, interpreting line fluxes and flux ratios for lines at different wavelengths is very difficult (it is known from Brα/Pfγ flux ratios that the H I lines are not well described by either the LTE or the Baker Menzel case B recombination assumptions – thus the Brα/Brγ ratio cannot be trusted as an indicator of the reddening [Höflich & Wehrse 1987]). Therefore, in our discussion, we prefer to focus on EWs, EW ratios (EWRs) and line shapes since these are not affected by reddening. For quantitative comparison, Table 2 gives a summary of the range of observed EW, FWHM and half-width-at-zero-intensity (HWZI) from Bunn et al. (1995). The table also gives the observed range of EWRs for Brα/Brγ and Brα/Pfγ[1]. Since our model parameters are not fine-tuned to one particular object, these values should be regarded only as indicative of the appropriate regime in which acceptable model predictions should lie.

4.2 Reference model (Model A)

Spectra have been computed in the 2 – 5 μm range using the reference wind model (Model A) which was described in Section 2. In this wavelength range, the model predicts moderately strong emission in the first three lines of the Brackett series and weaker emission in lines of the Pfund series (Pfβ and Pfγ). This is in qualitative agreement with the observed IR properties of massive YSOs (e.g. Simon et al. 1981,1983; Drew et al. 1993; Bunn et al. 1995).

[1] Hereafter, these EWRs will be referred to as EWR[Brα/Brγ] and EWR[Brα/Pfγ] respectively.

Figure 5 shows the predicted Model A line profiles of Brα, Brγ and Pfγ. Spectra are shown for a grid of viewing angles ranging from 30° to 85° (measured relative to the polar axis). For quantitative comparison with observations, the computed EW and FWHM of these lines are tabulated in Table 3. For completeness, computed line fluxes and flux ratios are given in Table 4.

For all three lines, the EW is largest for viewing angles ($\theta_{\rm obs}$) of 70 – 80° and becomes noticeably smaller at lower $\theta_{\rm obs}$. The computed Brα EWs are consistent with the high end of the range of measured EW (Table 2) obtained by Bunn et al. (1995). Similar agreement between observations and the model is also found for Pfγ making the modelled EWR[Brα/Pfγ] similar to the observed ratio.

For Brγ, the Model A computed EWs lie in the mid-range of the observed values (see Table 2). The relative weakness of the computed Brγ line means that the model EWR[Brα/Brγ] is systematically too high – in the observations the EWR for these lines ranges from 1.1 to 4.4 but the computed Model A ratio is somewhat higher, ranging from 11 to 13 for the viewing angles considered. It is probable that part of this disagreement is the result of opacities being too low in the models – but given the good agreement with observations for EWR[Brα/Pfγ], it seems unlikely that a simple underestimate of the opacity in Brα is solely responsible. Perhaps more importantly, the EWR[Brα/Brγ] will be affected by inaccuracies in the model continuum shape – since Brα and Pfγ lie at similar wavelengths, the choice of continuum shape will have little effect on the computed ratio of their EWs but because Brγ lies at a significantly shorter wavelength, the EWR[Brα/Brγ] is much more sensitive. An alternative treatment of the continuum – that invoking a reprocessing disk – is considered in Section 4.2. It is also noted

Table 3. Equivalent widths (EW) and full-width-at-half-maximum (FWHM) for the Brα, Brγ and Pfγ lines at different viewing angles ($\theta_{\rm obs}$). The values of FWHM have accuracy of around ~ 50 km s^{-1}, limited by the frequency gridding of the calculations. The accuracy of the EWs is limited by MC noise in the spectrum. Typically, the Monte Carlo noise in the continuum is < 2 per cent.

	$\theta_{\rm obs} = 30°$		$\theta_{\rm obs} = 45°$		$\theta_{\rm obs} = 60°$		$\theta_{\rm obs} = 70°$		$\theta_{\rm obs} = 80°$		$\theta_{\rm obs} = 85°$	
Line	$-$EW (Å)	FWHM (km s^{-1})	$-$EW (Å)	FWHM (km s^{-1})	$-$EW (Å)	FWHM (km s^{-1})	$-$EW (Å)	FWHM (km s^{-1})	$-$EW (Å)	FWHM (km s^{-1})	$-$EW (Å)	FWHM (km s^{-1})
Model A (reference model with reflecting disk)												
Brα	44	300	56	425	70	550	78	610	77	610	68	550
Brγ	4.0	290	4.9	420	5.6	520	5.8	520	5.8	550	5.4	550
Pfγ	7.2	340	9.3	450	12	560	13	560	14	560	13	560
Model B (reference model with reprocessing disk)												
Brα	3.1	430	4.2	610	6.1	730	8.5	790	14	790	19	790
Brγ^a	0.17	–	0.36	–	0.41	–	0.57	–	0.83	–	1.2	–
Pfγ^a	0.76	–	0.80	–	1.3	–	1.7	–	2.8	–	3.8	–
Model C (as Model B but with mass loss rate enhancement)												
Brα	27	300	38	425	56	550	74	550	100	670	120	670
Brγ	3.4	290	4.8	420	7.1	520	9.3	550	11	580	12	620
Pfγ	6.6	340	9.6	450	13	560	17	560	21	560	22	670
Model D (as Model A but with disk out to 100 r_*)												
Brα	24	300	32	425	43	550	53	550	62	610	63	550
Brγ	3.4	360	3.9	420	4.5	550	4.7	590	4.6	590	4.2	590
Pfγ	4.5	340	5.7	450	7.6	500	9.5	560	11	560	12	560
Model E (as Model C but with disk out to 100 r_*)												
Brα	4.6	300	6.6	430	10	550	16	610	29	670	49	670
Brγ	0.80	390	1.1	550	1.6	650	2.3	750	3.8	720	5.4	720
Pfγ	1.2	340	1.6	620	2.3	730	3.1	730	5.1	730	8.1	730
Model F (disk with inner hole, see Section 4.4)												
Brα	22	300	28	300	36	425	43	425	51	425	52	490
Brγ	2.2	260	2.4	360	2.6	460	2.7	490	2.7	490	2.5	490
Pfγ	2.8	220	3.8	340	5.0	450	6.2	450	7.5	450	7.9	450

[a] For Model B, the Brγ and Pfγ lines are very weak and only appear marginally above the MC noise – therefore, the entries for these lines give only upper limits on their EW.

that, compared with Brα and Pfγ, observations of Brγ for heavily embedded targets are more likely to be contaminated by emission from other sources (e.g. larger scale nebular emission) owing to the wavelength dependence of the source extinction.

The computed line profiles are complex, usually exhibiting double-peaks which become more pronounced at larger $\theta_{\rm obs}$. This is in contrast to the observations where only single-peaked profiles are usually observed (see Section 4.1). Also, the computed profiles are too broad (FWHM ranging from 300 to 600 km s^{-1} as a function of $\theta_{\rm obs}$). Part of this discrepancy between model and observations may be explained by contamination of the observed profiles by narrow nebular emission – there is some evidence for hybrid line profiles with narrow cores (see Section 4.1) – however, the half-width-zero-intensity (HWZI) measurements also suggest that the observed line profiles do not extend more than 200 to 300 km s^{-1} from line-centre in most cases.

The large line widths and double-peaked profiles arise due to the rotational velocities in the region of line formation. Figure 6 identifies the region of line formation for the Brα, Brγ and Pfγ lines in Model A; specifically, the plots show the amount of energy that escapes in each spectral line from each grid cell in the model. Note that MC noise is responsible for the graininess of the figures. It can be seen that in all three cases, the region of line formation is close to the disk surface, within the first few velocity law scale-lengths along the wind streamlines. Brα tends to form slightly further out than either Brγ or Pfγ – this is to be expected owing to the higher opacity in the Brα line.

To obtain models which produce narrower lines, either more low-velocity gas must be added, or high-velocity gas must be removed. The simplest way in which to introduce low-velocity gas is by increasing the outer disk radius ($r_{\rm disk}$) – models with wider disks are presented in Section 4.3. To remove high-velocity gas requires a reduction in the wind density at small values of r. Given that the inner disk is brighter than the outer disk, it seems unlikely that a radiatively driven flow will not have greatest mass-loading at small radii. Therefore, the most plausible way in which to eliminate high-velocity gas is not to change the prescription of mass-loading but rather to consider models in which either the stellar radius is larger than that adopted in the reference model or the disk inner radius is several times greater than the adopted stellar radius. An example of the latter, a model with an empty inner cavity in the disk, is discussed in Section 4.5.

To assess the relative importance of the disk wind and stellar wind component, results from a calculation considering only the disk wind component were compared with those which include the stellar wind. These two calculations give virtually identical results – this is not unexpected since it is already known that a spherical wind would require a mass-loss rate at least an order of magnitude greater than that in the stellar wind component here (Simon et al. 1981, see Section 1). In view of this, in all the calculations

Table 4. Computed Brα line fluxes and flux ratios Brα/Brγ and Brα/Pfγ at different viewing angles. Fluxes are given in units 10^{-13} ergs cm^{-2} s^{-1} for an unreddened source at a distance of 1 kpc.

	$\theta_{\rm obs} = 30°$	$\theta_{\rm obs} = 45°$	$\theta_{\rm obs} = 60°$	$\theta_{\rm obs} = 70°$	$\theta_{\rm obs} = 80°$	$\theta_{\rm obs} = 85°$
Model A (reference model with reflecting disk)						
Brα flux	5.1	5.3	4.9	4.3	3.3	2.6
Brα/Brγ	1.72	1.70	1.66	1.59	1.48	1.36
Brα/Pfγ	4.86	4.74	4.67	4.48	4.13	3.81
Model B (reference model with reprocessing disk)						
Brα flux	4.8	5.0	4.5	3.9	3.1	2.6
Brα/Brγ^a	1.99	1.37	1.73	1.72	1.85	1.72
Brα/Pfγ^a	3.07	4.09	3.34	3.84	3.65	3.77
Model C (as Model B but with mass-loss rate enhancement)						
Brα flux	43	47	43	37	27	20
Brα/Brγ	0.91	0.93	0.93	0.95	1.05	1.19
Brα/Pfγ	3.05	3.01	3.16	3.27	3.69	4.09
Model D (as Model A but with disk out to 100 r_*)						
Brα flux	4.0	4.1	4.0	3.6	3.0	2.5
Brα/Brγ	1.54	1.59	1.60	1.59	1.56	1.52
Brα/Pfγ	4.50	4.61	4.66	4.49	4.33	4.18
Model E (as Model C but with disk out to 100 r_*)						
Brα flux	25	26	25	23	19	16
Brα/Brγ	1.32	1.40	1.49	1.51	1.56	1.64
Brα/Pfγ	3.07	3.44	3.66	4.11	4.57	4.90
Model F (disk with inner hole, see Section 4.4)						
Brα flux	19	19	19	17	16	14
Brα/Brγ	2.37	2.37	2.29	2.18	2.06	2.03
Brα/Pfγ	6.94	6.20	5.82	5.60	5.17	4.93

^{a} For Model B, the Brγ and Pfγ lines are very weak and only appear marginally above the MC noise - therefore, the entries for these lines give only lower limits on the appropriate flux ratios.

discussed below, the stellar wind component is dropped for computational efficiency.

4.3 Reprocessing of radiation by the disk (Models B and C)

In Model A (discussed above) it was assumed that the photons striking the accretion disk were reflected rather than absorbed. To investigate an alternative simple hypothesis, namely that the disk absorbs and thermally re-emits the radiation which strikes it (see Section 2.2.2), a second model (Model B) is now considered. This is the extreme, optically thick disk case. All the system parameters (Table 1) for Model B are identical to those of Model A, saving that the stellar wind component is omitted (see above).

The simple treatment of reprocessing adopted (see Section 2.2.2) means that the disk is much brighter at IR wavelengths in Model B than Model A. Thus, although the wind parameters in Model B are unchanged, the EWs of all the emission lines are much smaller (the EWs are given in Table 3). At moderate to high $\theta_{\rm obs}$, the Model B EWs for Brα and Pfγ are comparable to the observed EWs in the weaker sources reported by Bunn et al. (1995). However, the computed Brγ line is very weak.

To increase the line EWs in the presence of a reprocessing disk the wind density (and hence emission measure) needs to be increased. Therefore, a further model (Model C) has been constructed – it is identical to Model B saving that the disk-wind mass-loss rate has been increased by a factor of four. A higher mass-loss rate may be feasible even under the assumption of driving purely by radiation since the absolute mass-loss rates provided by the hydrodynamical model of Drew et al. (1998) may be uncertain by a factor of a few owing to the parameterisation of the line-driving force. EWs and FWHM for Model C are given in Table 3 and the line profiles computed from this model are shown in Figure 7.

The Model C EWs are slightly greater than even the largest observed values from the Bunn et al. (1995) data, suggesting that the factor of four mass-loss rate increase between models B and C comfortably brackets the range of values that are likely to be consistent with the data for particular objects.

The EWR[Brα/Pfγ] is smaller for Model C than Model A, lying close to the mid-range of observed values. The EWR[Brα/Brγ] is also smaller in Model C – it is still greater than the observed ratio in any of the objects observed by Bunn et al. (1995) but the discrepancy is much less. This change in the line ratios is mostly due to the increased Brα opacity resulting from the higher wind density. This result suggests that by further increasing the mass-loss rate an EWR[Brα/Brγ] close to that observed could be achieved. However, it is noted that a further increase in the wind density will lead to Brα EWs which are uncomfortably large.

The Model C line profiles are generally less double-peaked and more square-topped than the Model A profiles. Their FWHM are very similar to those in Model A and the line wings still extend to several hundred km s^{-1} at the base.

In general, Model C appears to suggest that the combination of a reprocessing disk and a higher disk-wind mass-loss rate is in closer agreement with the observations than the reference model

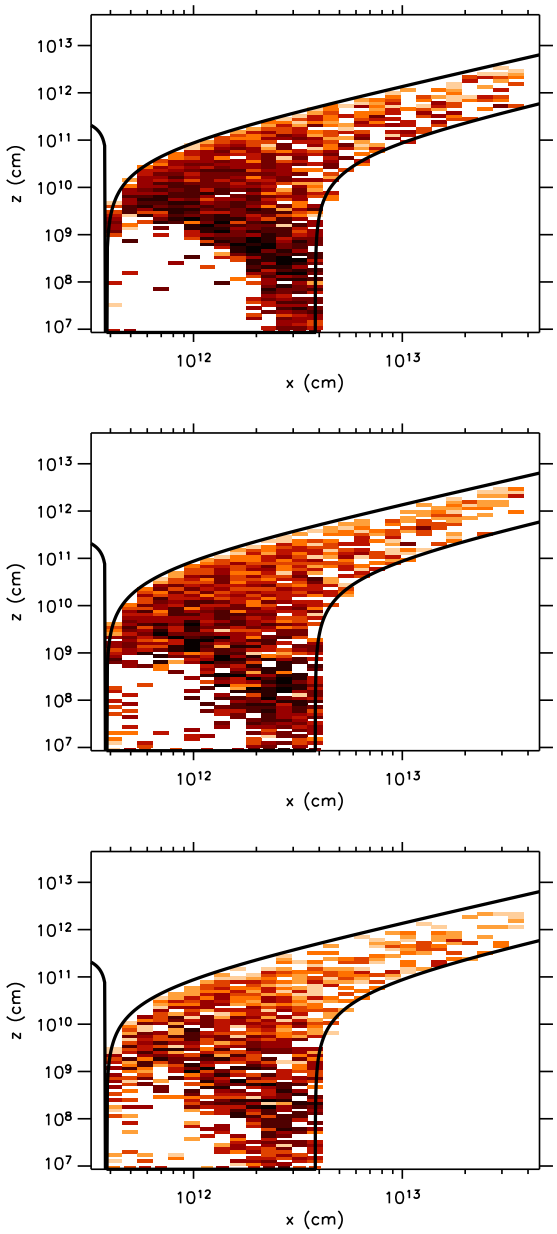

Figure 6. Regions of line formation for Brα (upper), Brγ (centre) and Pfγ (lower). Note the logarithmic axes. The solid black lines define the boundaries of the disk wind (the star surface, the disk surface and the inner and outer wind boundaries defined by $\theta_{\rm min}$ and $\theta_{\rm max}$). Within the wind, the volume is divided into the computational grid cells which are shaded proportional to the energy escaping to infinity from that cell in the spectral line under consideration. The shading scale is logarithmic. The graininess is due to MC noise.

(Model A). But further hydrodynamical modelling is required to examine whether so high a mass-loss rate is feasible.

4.4 The influence of the outer radius of the disk

The outer disk radius paralleling that of Drew et al. (1998) and adopted in Models A – C is, arguably, rather small. In principle, line formation in a wind rising from the outer parts of a larger disk could eliminate the double-peaked line shape obtained with Models A – C by adding low-velocity gas. In this section two more models (Models D and E) are considered: these models are identical, respectively, to Models A and C saving that the outer disk radius is set to 100 r_* rather than 10 r_*.

The computed line profiles for Model D are shows in Figure 8 and the EWs for Models D and E are given in Table 3. The differences between the profile shapes shown in Figures 5 and 8 are generally fairly small. The double-peaked shape is slightly filled in when the larger disk is considered; however, the assumption that the mass-loading of streamlines is proportional to the luminous flux (see Section 2.2.3) means that the majority of the mass-loss still originates from the inner disk where velocities are high. The most important consequence of the larger disk is the increase in the IR continuum level (see Figure 3 and the discussion in Section 2.3.2). The brighter continuum means that, when the disk is bigger, the line EWs are all smaller. Also, the EWR[Brα/Brγ] is smaller – the larger disk radius increases the continuum around 4 μm by more than at 2 μm (see Figure 3).

For Model D, the Brα EWs lie comfortably in the mid-range of the observed values and the EWR[Brα/Pfγ] is similar to that found in Model A. The EWR[Brα/Brγ] is smaller in Model D than A (as required) but the improvement is less significant than obtained with Model C (see Section 4.2). Model E predicts smaller EWs, but still within the range observed. The EWR[Brα/Brγ] in Model E is closer to that observed than in any of the other models – this follows since Model E benefits from the improvement in this ratio resulting from both a higher line opacity (density) and stronger disk continuum.

4.5 The influence of a central hole in the disk

It is apparent that a failing of Models A – E in comparison with the data is that the computed line profiles are too broad. One of two possible solutions to this problem is to invoke an inner hole in the accretion disk, thereby removing the highest velocity material from the region of line formation. Optically thin inner cavities in accretion disks around young luminous stars have previously been suggested in various contexts (e.g. Herbig Ae/Be stars – Dullemond et al. 2001; Tuthill, Monnier & Danshi 2001; Natta et al. 2001; and see Monnier et al. 2005 for a recent discussion). Interestingly, a disk with an inner hole might also help explain the residual discrepancy between the observed EWR[Brα/Brγ] and the models discussed above. Since the inner parts of the accretion disk are hottest, removing them will push the SED of the disk to the red. This will increase the continuum level at Brα relative to Brγ and therefore reduce the EWR[Brα/Brγ] as required. However, a quantitative investigation of this possibility goes beyond the scope of this paper since more sophisticated models for the disk emission than used here would be required.

Consideration of models in which the disk has a central hole represents a significant departure from the Drew et al. (1998) model and therefore, until further hydrodynamical calculations are performed, it is difficult to place useful constraints on the likely geometry and parameters for mass-loss from such a disk. Nevertheless, for illustrative purposes, a model adopting the same wind opening angles ($\theta_{\rm min}$, $\theta_{\rm max}$) and mass-loss rate as the reference model (Model A; Section 4.1) but with an inner disk radius of $r_{\rm in} = 5\ r_*$ and outer disk radius of $r_{\rm in} = 100\ r_*$ has been constructed (Model F) – this corresponds to a disk with a circular inner hole of ~ 0.1 AU. It is noted that, conceptually, invoking a wind launched significantly further out than the stellar surface is reminiscent of the photoevaporation model (e.g. Hollenbach et al. 1994) –

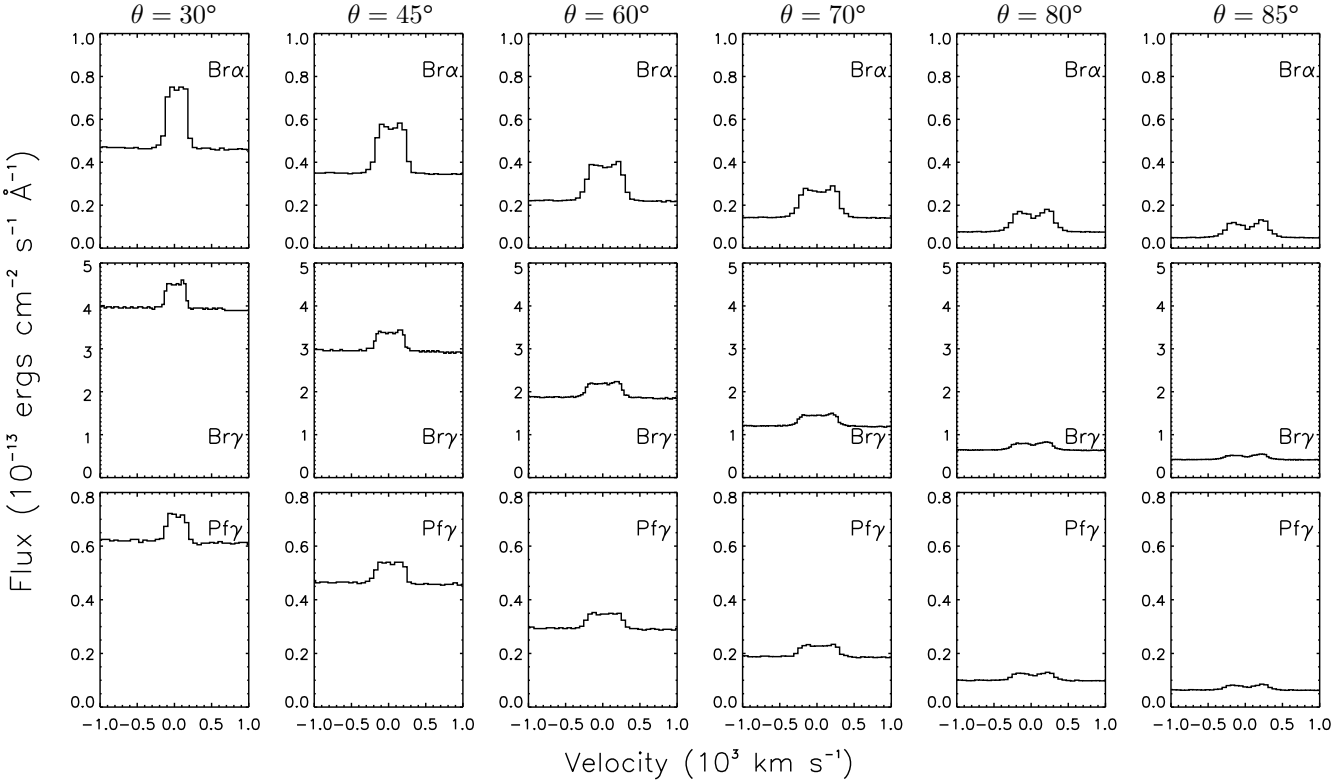

Figure 7. As Figure 5 but showing Model C (reprocessing disk, enhanced mass-loss rate) results.

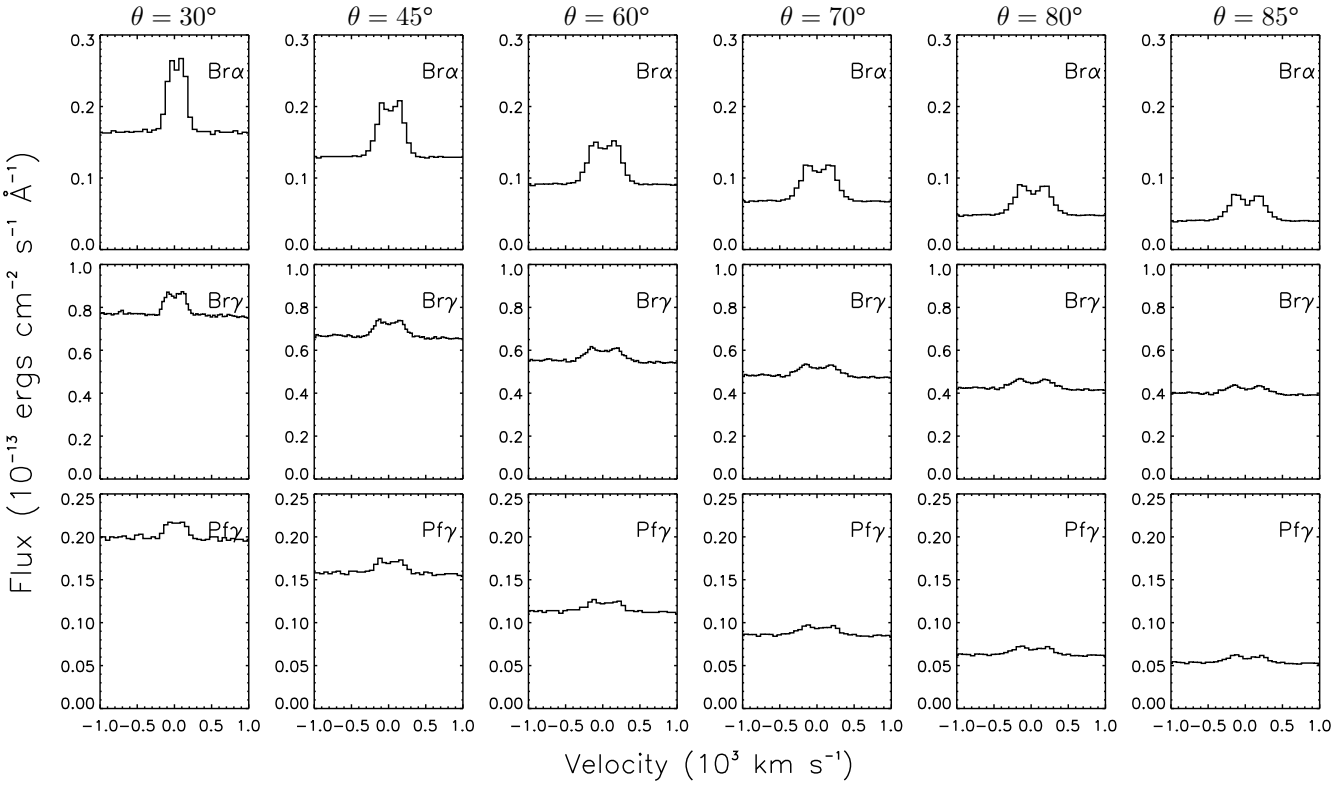

Figure 8. As Figure 5 but showing Model D (reflecting disk with larger outer radius) results.

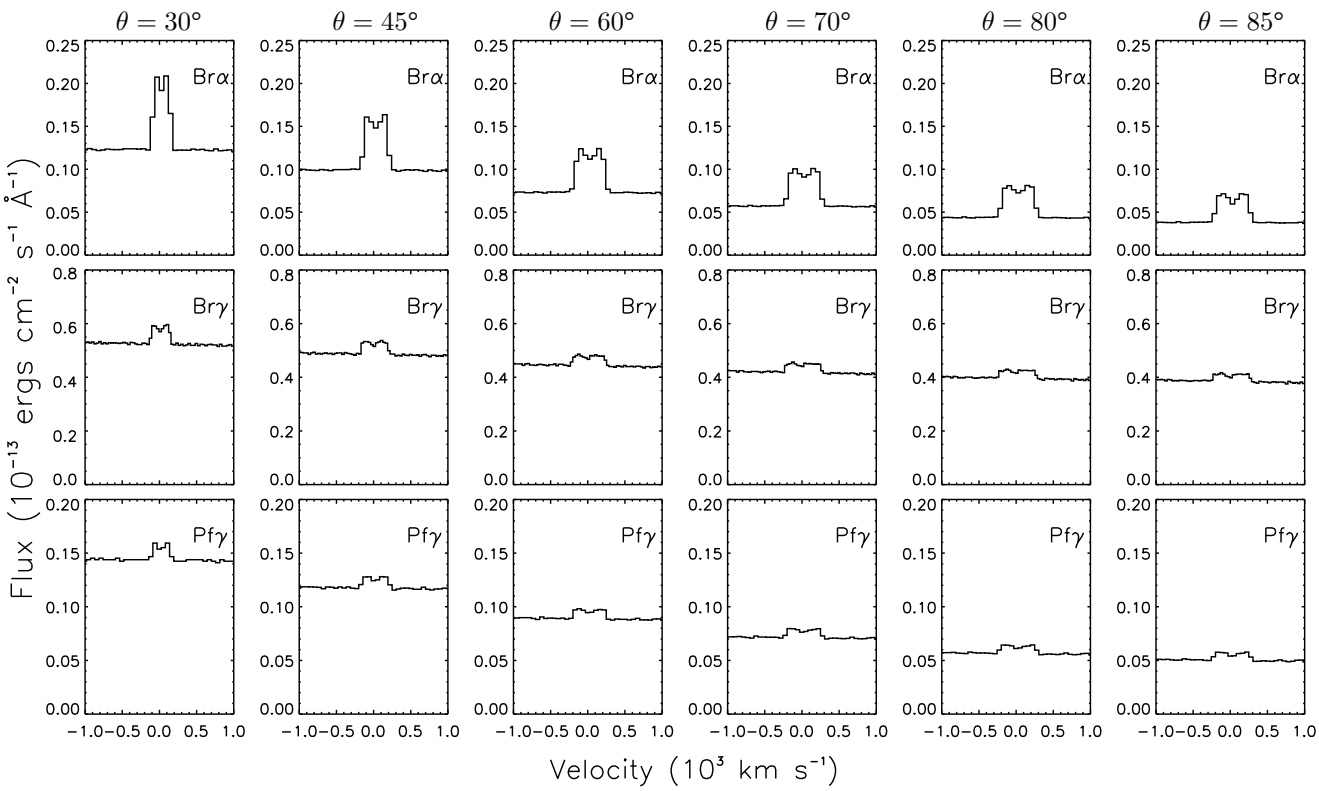

Figure 9. As Figure 5 but showing Model F (disk with inner hole) results.

however, the distance from the central star at which the mass-loss occurs here is still much smaller than expected from photoevaporation. It is, however, comparable to the smallest disk radii inferred from CO observations by Bik & Thi (2004).

The computed FWHM and EWs for Model F are tabulated in Table 3 and the profiles are shown in Figure 9. The EWs are smaller than those for Model A because the density in the wind is lower, a result of the radial dependence of the volume element in a cylindrical polar system. The lower density also leads to lower opacity and hence larger ratios of Brα to Brγ and Pfγ. However, as anticipated, the Model F lines are narrower than in Model A, by up to 100 km s^{-1} in FWHM for moderate inclination angles. The profile widths at base are also smaller – in Model F the profiles cut-off at $\sim$ 300 km s^{-1} from line centre. Thus holes of the size considered here, or a little larger, could explain why the HWZI measurements of Bunn et al. (1995) are rather smaller than would be expected based on Models A – E.

Given that there are no strong constraints on the hole size, geometry or mass-loss rate appropriate for the model here it is not possible to drawn definitive conclusions. However, it seems that models with an inner disk cavity have the potential to resolve the discrepancies between the computed disk wind line profiles and the observations. Model F also suggests that the second possibility mentioned in Section 4.2 – that of an enlarged stellar radius – can also provide a possible solution since increasing the stellar radius will affect the line widths in a similar way to introducing an inner gap in the disk. Constraints on the size of any inner hole, the stellar radius and the geometry of the disk wind are needed in order to proceed. These could be provided via sophisticated observational techniques such as interferometry (which has already been applied to Herbig Ae/Be stars by e.g. Monnier et al. 2005) or spectropolarimetry (as discussed by Vink, Harries & Drew 2005).

5 DISCUSSION

As mentioned in Section 4, direct confrontation of theoretical line fluxes with observations is difficult owing to the uncertainty in the extinction along lines-of-sight to massive YSOs. But on comparing EWs – the quantities most readily extracted from observations – the radiative transfer calculations presented above lead us to conclude that model disk winds, such as that obtained by Drew et al. (1998), do predict H I line strengths consistent with observations of massive YSOs. This matching is achieved for total mass-loss rates between 0.3 and 1.2 $\times 10^{-7}$ M$_\odot$ yr^{-1}, in contrast with previously calculated spherical models for early B stars which require mass loss rates up to 10^{-6} M$_\odot$ yr^{-1} (Simon et al 1983, Nisini et al 1995).

There are, however, some difficulties when the models are considered in detail. Although the computed EWR[Brα/Pfγ] agrees well with observations, the EWR[Brα/Brγ] tends to be overpredicted by the models. We have investigated the effect of a higher density on this ratio by considering models with greater mass-loss rate (e.g. Model C; recall that the model density is sensitive to several parameters in addition to the mass-loss rate and thus there is a degree of degeneracy among these quantities – see Section 2.3.5). As expected, increasing the wind density decreases the EWR[Brα/Brγ] owing to the greater optical depth. However, to fully explain the EWR discrepancy solely by such a modification is difficult since the absolute values of the EWs grow rapidly if the density is raised. At the same time, this EWR is very sensitive to the assumed underlying SED, owing to the significant wavelength dif-

ference between the Brα and Brγ lines (unlike Brα and Pfγ which lie at similar wavelengths). Observationally it is clear that there is genuine diversity in the IR SEDs of massive YSOs (e.g. Henning et al. 1990). In our models we have considered only two limiting cases for the treatment of the SED and have not concerned ourselves with trying to fit specific objects. To determine whether the EWR[Brα/Brγ discrepancy is unavoidable, there is now a need to move on to fitting observations of individual well-observed sources with reliable reddening estimates.

Important differences are also evident in comparisons of the line profiles obtained from our models and those typically observed in massive YSOs. To illustrate this, Figure 10 compares the observed Brα profile for GL989 (taken from Bunn et al. 1995) with computed profiles from two of the models. GL989 is chosen here since the line profiles for this object have strong extended wings and, in contrast to several of the other objects in the Bunn et al. (1995) sample (e.g. S106IR), have simple profiles suggesting a single dominant region of line formation. The comparison models and viewing angles (Model B with $\theta_{\rm obs} = 60°$ and Model E with $\theta_{\rm obs} = 45°$) were selected since they predict Brα EWs close to the observed value, thereby allowing a direct comparison of profile shape.

The figure shows that the Model B Brα profile at $\theta_{\rm obs} = 60°$ is too broad and, in contrast to the observations, is double-peaked. The Model E profile ($\theta_{\rm obs} = 45°$) is in better agreement with the observation – the combination of higher optical depth in the model (owing to the increased mass-loss rate) and lower viewing angle reduce the profile width and suppress the double-peaks – but a significant discrepancy remains. To resolve this difference in line shape between the models and typical observations, one could invoke even smaller inclination angles. Although viewing angles are not known for most luminous YSOs, this is not an attractive solution since small viewing angles (close to pole-on) are statistically disfavoured in an unbiased sample. Furthermore, at least one of the objects discussed by Bunn et al. (1995) is known to be viewed almost edge-on (S106IR; Solf & Carsenty 1982). Thus we prefer to pursue resolutions to the two styles of line shape discrepancies which do not rely on orientation effects.

Increasing the physical extent of the disk from which the wind is launched does not readily eliminate the double-peaked line shape from our models (Models D and E) – although some of the wind does occupy regions with lower rotational velocities when the disk is made larger, our assumption that the mass-loading is proportional to the luminous flux of the disk means that most of the mass in the wind is still launched at small radii. The problem of reconciling observed single-peaked line profiles with theoretical predictions of double peaks has arisen elsewhere, particularly in studies of nova-like variables (see e.g. Horne 1997) and active galactic nuclei (AGN). In the context of AGN, Murray & Chiang (1997) have argued that substantial radial velocity shear in a disk wind can suppress the formation of double-peaked profiles as required. For this to occur, it is necessary that line optical depths are high such that photon escape is strongly favoured in the poloidal direction where accelerating outflow ensures steep velocity gradients. It is this difference between Model C, with enhanced mass loss, and Model A that explains the relatively flat-topped profiles in Fig. 7, compared to Fig. 5. Hence there is scope to re-organise model parameters in order to exploit this mechanism to suppress double peaks. In particular, a way of raising line opacity without also raising Brα EWs is needed. This will warrant further investigation in future work, focusing on fitting observations of specific objects.

Some of the discrepancies, in particular the large linewidths predicted by the models, may be explained by departures from the particular disk wind geometry adopted (which was motivated by the Drew et al. 1998 model). Two interesting possibilities are those of an enlarged radius for the central star, relative to a main-sequence radius, or of an inner gap in the YSO disk. These possibilities have rather similar consequences – by moving the disk wind out to larger radial distances from the central object, the correspondingly lower rotation velocities reduce the extent of the line wings and make the double-peaks less prominent (this is illustrated by our model with a cavity in the inner disk, Model F). Also, the SED for a disk with a hole will be redder than that for a complete disk, helping to explain the EWR[Brα/Brγ] discrepancy. These alternatives might be distinguished by observational techniques that probe the inner disk geometry (e.g. interferometry and spectropolarimetry) while the influence of a gap on the SED needs to be investigated fully in subsequent work incorporating more sophisticated treatments of the disk SED than used here.

A third possibility is that of disk winds in which the streamlines diverge less at large distances. In our models, the divergence of the streamlines is imposed by our adopted "split dipole" geometry. In a geometry with less divergence of the flow, the density would be higher in the outer parts of the wind for a given mass-loss rate and velocity law. The increased emission measure at large radii would help to wash out the double-peaked profiles which form when the emission is dominated by gas in rotation close to the central object. For appropriate viewing angles, line-of-sight optical depths would also be larger for a less divergent outflow. As has already been noted, higher optical depths present a promising solution to part of the EWR[Brα/Brγ] discrepancy. Thus, in the context of studying particular objects in detail, considering a range of different disk wind geometries is likely to prove fruitful in future work.

These issues aside, the major success of our radiative transfer simulations is their support of the hypothesis that disk winds can play a significant role in creating the H I lines of massive YSOs. In particular, the departure from one-dimensional wind models has alleviated the need to invoke the uncomfortably large mass-loss rates required in earlier spherical models. Further investigations of the applicability of the disk wind model to particular objects are now warranted.

ACKNOWLEDGEMENTS

SAS thanks L. Lucy for several useful discussions relating to this work and L. Mendes for technical support in use of the Imperial College Astrophysics Beowulf cluster.

This work was undertaken while SAS was a PPARC supported PDRA at Imperial College London (PPA/G/S/2000/00032).

REFERENCES

Bik A., Thi W. F., 2004, A&A, 427, L13
Blum R. D., Barbosa C. L., Damineli A., Conti P. S., Ridgway S., 2004, ApJ, 617, 1167
Bonnell I. A., Vine S. G., Bate M. R., 2004, MNRAS, 349, 735
Bunn J. C., Hoare M. G., Drew J. E., 1995, MNRAS, 272, 346
Carr J. S., 1989, ApJ, 324, 522
Carr J. S., Tokunaga A. T., Najita J., Shu F. H., Glassgold A. E., 1993, ApJL, 411, L37
Castor J. I., Abbott D. C., Klein R. I., 1975, ApJ, 409, 429

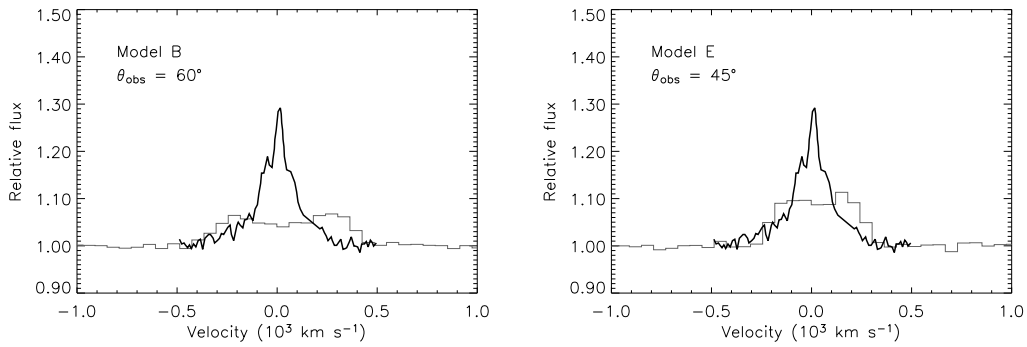

Figure 10. Comparison of the observed Brα profile for GL989 (taken from Bunn et al. 1995; heavy line) with computed profiles from Model B (for viewing angle of 60°; light histogram on left) and Model E (for viewing angle of 45°; light histogram on right). These models and angles have been chosen for comparison of profile shapes since they give Brα equivalent-widths which are similar to that observed for GL989. We show Brα only – since there are discrepancies between the modelled and observed EWRs (see text), the models shown significantly underpredict the Brγ-EW and therefore do not simultaneously allow useful comparisons of line shapes for all lines. Comparing the observed Brγ or Pfγ profiles to models which reproduce their EWs leads to the same conclusions obtained from considering Brα only.

Chandler C. J., Carlstrom J. E., Scoville N. Z., Dent W. R. F., Geballe T. R., 1993, ApJ, 412, L71
Chandler C. J., Carlstrom J. E., Scoville N. Z., 1995, ApJ, 446, 793
Cunto W., Mendoza C., Ochsenbein F., Zeippen C. J., 1993, A&A, 275, L5
Drew J. E., Bunn J. C., Hoare M. G., 1993, MNRAS, 265, 12
Drew J. E., Proga D., Stone J. M., 1998, MNRAS, 296, L6
Dullemond C. P., Dominik C., Natta A., 2001, ApJ, 560, 957
Hamann F., Simon M., 1986, ApJ, 311, 909
Henning Th., Pfau W., Altenhoff W. J., 1990, A&A, 227, 542
Höflich P., Wehrse R., 1987, A&A, 185, 107
Hollenbach D., Johnstone D., Lizano S., Shu F., 1994, ApJ, 428, 654
Horne K., 1997, in Wickramasinghe D. T., Bicknell G. V., Ferrario L., eds, IAU Colloquium 163, ASP Conference Series, Vol. 121, p.14
Knigge C., Woods J. A., Drew J. E., 1995, MNRAS, 273, 225
Kraus M., Krügel E., Thum C., Geballe T. R., 2000, A&A, 362, 158
Long K. S., Knigge C., 2002, ApJ, 579, 725
Lucy L. B., Abbott D. C., 1993, ApJ, 405, 738
Lucy L. B., 2002, A&A, 384, 725
Lucy L. B., 2003, A&A, 403, 261
Menzel D. H., Pekeris C. L., 1935, MNRAS, 96, 77
Mihalas D., 1978, Stellar Atmospheres (2nd Edition; San Francisco: Freeman)
Monnier J. D. et al., 2005, astro-ph/0502252
Murray N., Chiang J., 1997, ApJ, 474, 91
Natta A., Prusti T., Neri R., Wooden D., Grimm V. P., Mannings V., 2001, A&A, 371, 186
Proga D., Stone J. M., Drew J. E., 1998, MNRAS, 295, 595
Proga D., Stone J. M., Drew J. E., 1999, MNRAS, 310, 476
Simon M., Righini-Cohen G., Fischer J., Cassar L., 1981, ApJ, 251, 552
Simon M., Felli M., Cassar L., Fischer J., Massi M., 1983, ApJ, 266, 623
Solf J., Carsenty U., 1982, A&A, 113, 142
Tuthill P. G., Monnier J. D., Danchi W. C., 2001, Nature, 409, 1012
van Regemorter H., 1962, ApJ, 136, 906
Vink J. S., Harries T. J., Drew J. E., 2005, A&A, 430, 213